JOURNAL OF SOLID STATE CHEMISTRY 34, 323–333 (1980)

Shape Effects on Crystallite Size Distributions in Synthetic Hematites from X-Ray Line-Profile Analysis

P. H. DUVIGNEAUD AND R. DERIE

Chef de Travaux, Service de Chimie Industrielle et de Chimie des Solides, Université Libre de Bruxelles, Brussels, Belgium

Received June 7, 1979; in revised form November 6, 1979

Synthetic acicular hematite shows a nonuniform broadening of the X-ray lines in a wide temperature range. The factors affecting the peak broadening were studied by recording the powder line profiles of the (012), (104), (110), (024), and (116) reflections. The orientation relationships of these planes vs the main particle axes were previously checked by electron microdiffraction. On the other hand, various hematites having different particle sizes and shapes (spheres, slabs, needles) were investigated as well. The mean crystallite sizes were determined from a classical Fourier transform analysis whereas the size distributions were computed by a smoothing procedure described by A. Le Bail and D. Louër (*J. Appl. Crystallogr.* **11**, 50–55, 1978). The results show that the nonuniform broadening is ascribed to the shape anisotropy of the particles rather than to strains and faults broadening since (i) this last phenomenon is negligible in spherical-shaped particles, (ii) nonuniform broadening remains in acicular particles after further heating at 600°C, and (iii) a good estimate of the ratio of the particle width and thickness has been found.

Introduction

It is well known that the acicular crystals of goethite (αFeOOH) can undergo some transformations (dehydration, reduction, reoxydation) yielding successively hematite (α-Fe_2O_3), Magnetite (Fe_3O_4), and magnetic maghemite (γ-Fe_2O_3) without consequent changes of crystal size and shape. The topotactic characters of these reactions have been shown by several authors (*1–6*).

During the dehydration of goethite, hematite is formed in a close orientation relationship with the original goethite, the *a*, *b*, *c* axes of the orthorombic cell of goethite becoming *c*, *a*, and (1$\bar{1}$0) directions of the pseudohexagonal cell of hematite. A nonuniform broadening of the powder lines of hematite is often observed. As this effect decreases on further heating, some authors (*3–5*) believe that this nonuniform broadening is correlated to some crystal imperfections, strains, or faults occurring at low temperature. However, it is obvious that the anisotropy of the acicular crystals of goethite should lead to large differences in crystallite size depending on orientation of the diffracting planes with respect to the needle dimensions.

Recent progress in the X-ray analysis of broadening profiles at present enables:

(i) separation of stain broadening from crystallite size broadening by the Warren–Averbach method when multiple first orders of an *hkl* reflection are available;

(ii) determination of the mean crystallite sizes and size distributions normal to the

0022-4596/80/120323-11$02.00/0

diffracting planes. However, in order to test the self-consistency of these methods, it is suitable in practice to refer to well-characterized samples. Therefore different samples of hematite ranging from colloidal spheres to acicular particles have been selected and some of these have been heated in the temperature range 300–600°C. Particle sizes and shapes were determined by electron microscopy while complementary informations about the orientation of crystallographic axes versus particle dimensions were obtained by electron microdiffraction.

The X-ray reflections (104), (110), (024), and (116) were selected because:

(i) They represent different directions and consequently have a nonuniform broadening,

(ii) They are easily available in practice because the overlapping of the tails of the neighboring reflections is weak.

Samples

Four different samples were studied.

1. *Colloidal hematite A* (Fig. 1a) is obtained by slow hydrolysis of a heated solution of Fe(III) nitrate. The particle size distribution is normal, the average size $\bar{d}$ is 305 Å and σ is 80 Å. The particles are spherical-shaped.

2. *Colloidal hematite B* (Fig. 1b) is obtained by calcination at 300°C of a poorly crystallized sample of goethite which has been prepared from a solution of $FeSO_4$ under a NH_3–O_2 gas flow. The particle size distribution is log normal ($\bar{d}$ = 145 Å; log d(Å) = 2.13 and log σ = 0.16). The particle shape is ovoid but the ratio of maximal and minimal dimensions does not exceed 1.5.

3. *Tabular hematite C* (Fig. 1c) is obtained by calcination at 300°C of a poorly crystallized goethite which has been prepared by mixing a $NaOCl$–Na_2CO_3 solution with a hot $FeSO_4$ solution. The particle shape is irregular and not well defined. The ratio of particle length and width lies between 1.5 and 3. The mean diameter is about 360 Å.

4. *Acicular hematite D* (Fig. 1d) is obtained by calcination at 300°C of a commercial goethite. The needle lengths reach a few micrometers whereas the average "diameter" is 330 Å. One sample was heated at 600°C and another one was subjected to elutriation so that the finest particles (85 wt%) were eliminated. A narrower particle size range ($\bar{d}$ = 1000 Å) was selected and heated at 600°C as well.

Electron Microscopy and Electron Microdiffraction

The hematite lattice cell is rhombohedral. However, it is generally indexed in the hexagonal system with a = 5.038 Å and C = 13.77 Å (*4*). When isolated acicular crystals are examined by electron microdiffraction, the six spots of the (110) and (300) planes are frequently observed. Therefore, (i) the c axis of hematite is normal to the sample plane; (ii) the needles are slab-shaped. This has been confirmed by shading the sample plane at a 45° angle with carbon. The comparison of crystal and shadow dimensions shows that the needle width is about twice the corresponding thickness.

The orientation of the a_1, a_2, and a_3 axes normal to the c axis is shown in Fig. 2. Therefore the orientation of the (110), (104), (024), and (116) planes is known. The (110) planes are perpendicular to the a_1, a_2, and a_3 axes. Thus the (110) crystallite size should be equal to the needle width d for one-third of the planes whereas the other two-thirds correspond to d/sin 30°, i.e., 2d.

The (104), (024), and (116) planes, because of their high l index rather expresses a function of the needle thickness. The angle ϕ between the (hkl) and the basic

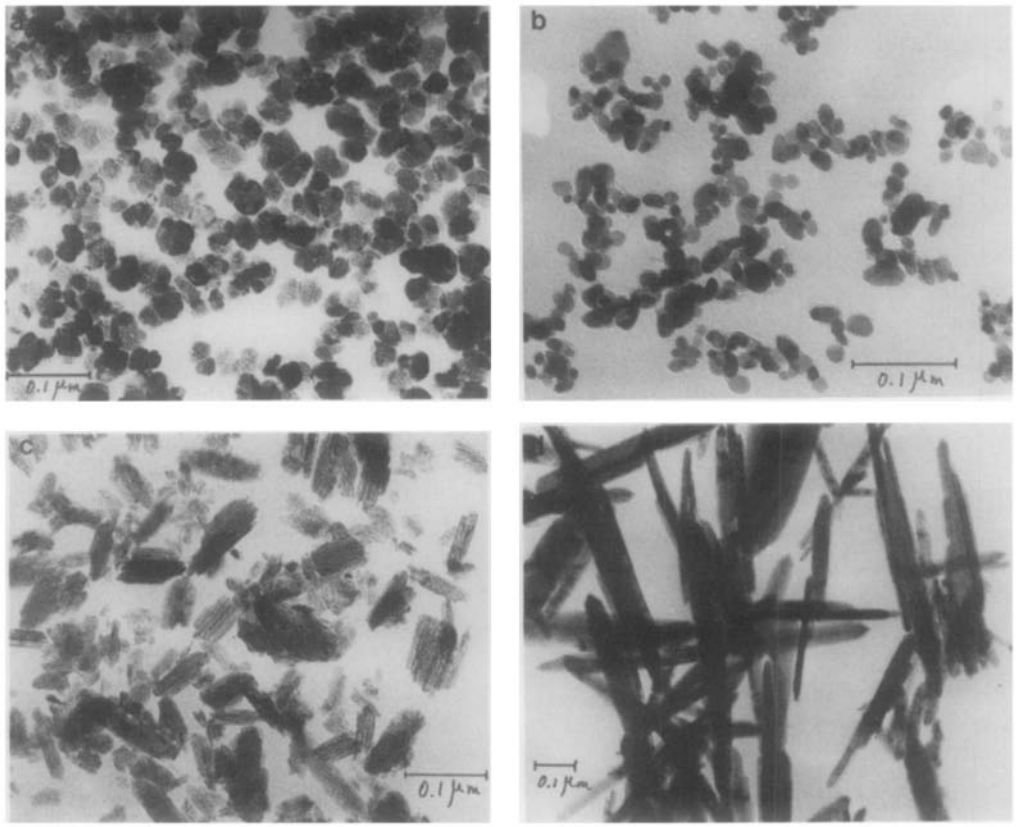

FIG. 1. (a) Colloidal hematite A. (b) Colloidal hematite B. (c) Tabular hematite C. (d) Acicular hematite D.

plane (001) is given by

$$\cos\phi = \frac{\frac{3}{4}a^2/c^2 l}{\frac{3}{4}a^2/c^2(h^2 + h^2 + hk + \frac{3}{4}a^2/c^2 l^2)} \quad (1)$$

and the (hkl) crystallite size is given by $t/\cos\phi$, where t is the needle thickness. Hence, ϕ is, respectively, 38°, 42°, and 58° for (104), (116), and (024) reflections so that the corresponding crystallite sizes are $1.27t$, $1.35t$, and $1.89t$ if the "edge" effects are neglected.

X-Ray Analysis

Method

If no strains are present in the material, the cosine Fourier coefficients $A(L)$ of the "true" diffraction line profiles enable the determination of two types of crystallite size distributions (*8*, *9*).

(i) The discrete function P(L) represents the numerical fraction of unit cell columns of length L normal to the diffracting planes

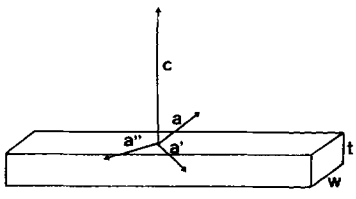

FIG. 2. Orientation of hexagonal axes in acicular hematite: The a axis is parallel to the needle width w. t is the needle thickness.

(*hkl*). L is related to the order number n of the coefficient by (*10*)

$$L = na_3' = \frac{n\lambda}{2(\sin\theta_2 - \sin\theta_1)} = \frac{n\lambda}{\Delta(2\theta)\cos\theta} \quad (2)$$

where θ_2 and θ_1 are the Bragg angles corresponding to the ends of the observation range.

$P(L)$ is characterized by its mean value

$$\bar{M} = \frac{\sum_{L=0}^{M} LP(L)}{\sum_{L=0}^{M} P(L)}, \quad (3)$$

where M is the maximal height of the columns.

(ii) The discrete function $G(L)$ represents the crystallite size volume distribution and is defined by

$$G(L) = \frac{LP(L)}{\bar{M}}. \quad (4)$$

Its mean value is

$$\bar{M}_1 = \frac{\sum_{L=0}^{M} L^4P(L)}{\sum_{L=0}^{M} L^3P(L)}. \quad (5)$$

The mean particle size $\bar{M}$ is given by the negative initial slope of the $A(L)$ curve plotted vs L:

$$\frac{1}{\bar{M}}(hkl) = -\frac{dA(L)}{dL}. \quad (6)$$

The mean particle size $\bar{M}_1$, also called integral breadth particle size coefficient, is related to the profile integral breadth β by the Sherrer relation (*11*)

$$\bar{M}_1 = \frac{1}{\beta} = \int_{-\infty}^{+\infty} A(L)dL \quad (7)$$

and is determined by the area under the $A(L)$ curve. As far as the "hook effect" arising from profile truncation is weak, the mean sizes $\bar{M}$ and $\bar{M}_1$ are significant and can be obtained from the classical Fourier transform analysis (FTA) by the "Stokes" method (*12*). However, $\bar{M}_1$ is less sensitive to the "hook effect" and is relatively stable despite the spurious oscillations in the $A(L)$ curves proceeding form the errors propagated through counting statistics, sampling factors (number of spaced points, angular range, estimation of background), and finite summation in deconvolution (*13*).

On the other hand, the Stokes Method is not suitable for calculating the distribution functions $P(L)$ and $G(L)$ because of the oscillating character of the $A(L)$ curves. In fact, $P(L)$ is given by the second derivative of the Fourier transform (*7, 8*) which is calculated in practice by (*14*)

$$P(n) = \frac{A_{n+1} - 2A_n + A_{n-1}}{A_0 - A_1}. \quad (8)$$

During the last few years several authors proposed some smoothing procedures for correcting the size distribution functions (*15–19*). In the present work, we have applied the least-squares procedure with a stabilization scheme described by Le Bail and Louër (*19*). In this method no particular analytical expression is assumed for the X-ray line profile. The broadening function is correlated to the crystallite size distribution $P(n)$ by

$$f(x) = \frac{1}{\langle N\rangle}\sum_{n=1}^{1} P(n)\frac{\sin^2(\pi nx/a)}{\sin^2(\pi x/a)}, \quad (9)$$

where $\langle N\rangle$ is the average number of cells in a column. $f(x)$ is discrete and defined by $(a + 1)$ points. Expression (9) constitutes a set of linear equations which can be written in a matrix form:

$$(A_{ik})_{(N\times l)}(P_k)_{(l\times 1)} = (f_i)_{(N\times 1)} \quad (10)$$

The vector solution (P_k) has coefficients $P(1), P(2), \ldots, P(l)$ and can be obtained with the Gauss–Siedel iterative method.

The corrected $P(n)$ values are compared to those of Eq. (8). If strains are present and cause broadening, this latter can be separated from particle and fault broadening by the Warren–Averbach method (7) when multiple first orders of a reflection are available. For small values of L and residual strain $\langle \epsilon_L \rangle$, we can write

$$\ln A(L) = \ln A^{PF}(L) - 2\pi^2(\langle \epsilon_L{}^2 \rangle - \langle \epsilon_L \rangle^2)L^2Sb^2. \quad (11)$$

Plotting $\ln A(L)$ vs the square of the variable $Sb = 2 \sin \theta_b/\lambda = 1/d_b(hkl)$, where the subscript b is related to the deformed sample and extrapolating to $Sb^2 = 0$ yields the particle-fault coefficient $A^{PF}(L)$ for different values of L. The slope of the extrapolation curve is a measure of the mean square strain $\langle \epsilon^2{}_L \rangle - \langle \epsilon_L \rangle^2$.

Experimental Procedures

The X-ray apparatus is a CGR 2080 diffractometer. The Co$K\alpha_1$ radiation of $\lambda = 1.7889$ Å is used. The $K\alpha_2$ line is reduced to $<5\%$ of the $K\alpha_1$ by a front quartz monochromator. A proportional counter with a pulse height discriminator is used. A step-scanning device coupled with an automatic printer enables us to count and record angular steps of 0.01° (2θ) for the apparatus profile $h(x)$ in a 6° (2θ) angular range and angular steps of 0.02° (2θ) in the same angular range for the broadened profiles. The "apparatus" profile is recorded from an analytical grade Fe_2O_3 "Merck" annealed at 1000°C.

A first computer program written in Fortran IV reads the $h(x)$ and $g(x)$ profiles, performs a smoothing of these data by a least-squares method fitting a parabolic curve through seven points, i.e., $h_{i-3} \ldots h_i \ldots h_{i+3}$, corrects for Lorenz-polarization factors, subtracts the background, and computes by a Stokes–De Angelis method (*20*) the cosine and sine Fourier coefficients of the "true" profile $f(x)$ using 50 half-harmonics. A first determination of the two mean particle sizes $\bar{M}$ and $\bar{M}_1$ is obtained by this method.

A second Fortran program computes the corrected particle size distributions $P(M)$ and $G(M)$ by the Louër–Le Bail method (*19*) from symmetrized $f(x)$ data. The mean particle sizes $\bar{M}$ and $\bar{M}_1$ of the corrected distributions are in agreement within ±5% with the values calculated from the previous program.

Experimental Results

Validity Test of the Method: Comparison between the "Microscopic" and "X-Ray" Particle Size Distributions of Colloidal Hematite A

In order to compare the "microscopic" and "X-ray" mean particle sizes and distributions, one has to keep in mind that the X-rays "see" the particles as multiple unit cell columns so that the mean crystallite size of a perfect homogeneous sphere is less than its true diameter. It is well known (*21*) that $\bar{M}_1 = 0.75D$ and $\bar{M} = 0.67D = 0.89\bar{M}_1$ for a sphere of diameter $D = 2R$. The volume fraction of columns of length L/R ($0 < L < 2R$) crossing the sphere is given in Table I. As the "microscopic" diameter distributions have been previously determined (with $\bar{D} = 305$ Å and $\bar{D}_1 = 365$ Å) it is possible, from these data and from Table I, to calculate a theoretical "X-Ray" crystallite size distribution. This is shown in Fig. 3. On the other hand, the Fourier coefficient curves $A(L)$ versus L of the (110), (104), (116), and (024) reflections (Fig. 4a) look similar so that (i) the isotropic character of the particles is confirmed, (ii) oriented strain broadening is negligible. The (024) crystallite size distribution $G(L)$ is matched with the theoretical one in Fig. 3. Although the former distribution is wider than the latter, an excellent agreement is

TABLE I

VOLUME FRACTION OF COLUMNS CROSSING A SPHERE AS A FUNCTION OF MEAN COLUMN LENGTH l ($0 < l < 2R$)

l	vol%
$0.1R$	0.1
$0.3R$	0.7
$0.5R$	1.9
$0.7R$	3.7
$0.9R$	6.1
$1.1R$	9.1
$1.3R$	12.7
$1.5R$	16.9
$1.7R$	21.7
$1.9R$	27.1

observed between the mean "crystallite" and "microscopic" sizes which are very close together (265 and 260 Å).

A more direct comparison of the mean crystallite size $\bar{M}_1$ ($\simeq 260$ Å from Table II) and the mean "volume" diameter $\bar{D}_1$ (345 Å) confirms the agreement between the "X-Ray" and "microscopic" sizes since the $\bar{M}_1/\bar{D}_1$ ratio is close to 0.75. From these results the particles of colloidal hematite A can be considered as isotropic single crystallites. However, the $\bar{M}/\bar{M}_1$ ratio, calculated from the data of Fig. 4a, is between 0.6 and 0.7. Such a ratio can be expected more in cubic-shaped particles (where, for example, $\bar{M}/\bar{M}_1$ reaches 0.66 for (111) planes) than in spheres. As a matter of fact, the electron microscope confirms (Fig. 1a) that the particles of colloidal hematite A are polyhedrons rather than perfect spheres.

Size Anisotropy Effects in Other Hematites

Colloidal Hematite B

The A(L) curves of the (104), (116), and (024) reflections are very similar (Fig. 4b) and give mean particle sizes $\bar{M}_1$ ranging from 120 to 140 Å (Table II) whereas the (110) Fourier coefficients lead to larger values of the $\bar{M}_1$ particles sizes (190 Å). Similar results are obtained from the mean values $\bar{M}$, as previously reported (*22*).

Tabular Hematite C

The broadening difference between (110) and the other reflections becomes larger in this sample as shown in Fig. 4c. Moreover, the broadening of the (024), (116), and (104) reflections become nonuniform and leads to different crystallite sizes (Table II).

Acicular Hematite D

The nonuniform broadening is emphasized in this hematite which shows more crystallite size differences in the studied directions than the previous ones. Particular attention will be given to this hematite in order to interpret the observed anisotropy of broadening (Fig. 4d).

Mean Crystallite Sizes

The mean dimensions $\bar{M}_1$ obtained from samples heated (i) at 300°C, (ii) at 600°C, and (iii) at 600°C after elutriation are reported in Table II. It is assumed first that no strain broadening occurs.

At 300°C and at 600°C as well, the (110) crystallite sizes are larger than the other (*hkl*) dimensions. However, at 600°C, the differences between the former and the latter become less important.

First of all, the (110) size change from 300°C (i) to 600°C (ii) is weak and confirms

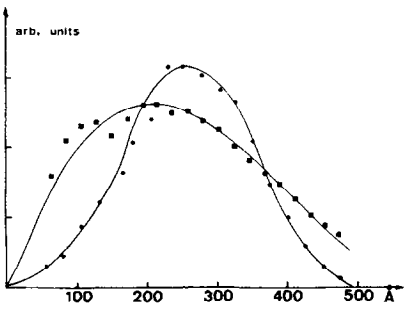

FIG. 3. Calculated crystallite size distributions in colloidal hematite A: ●, From electron microscopy; ■, from X-ray analysis of (024) reflection.

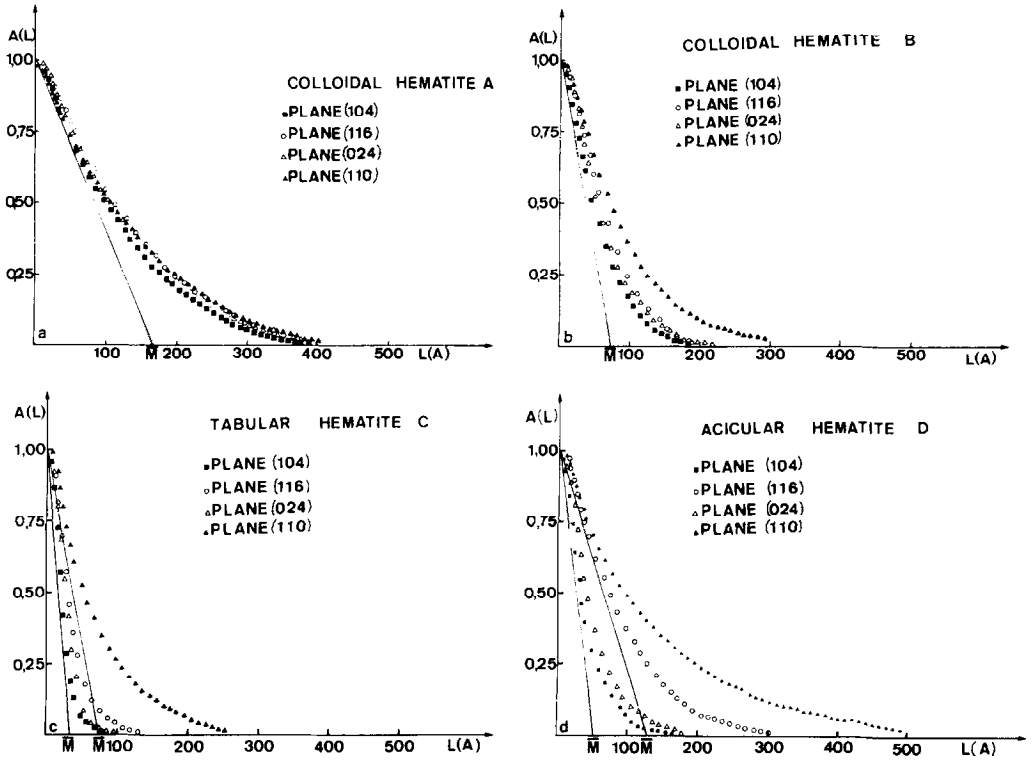

FIG. 4. Fourier coefficients $A(L)$ of hematite samples as a function of L.

that the "microscopic" needle dimensions are not modified in this temperature range. As reported above, the (110) mean dimension $\bar{M}_1$ should be theoretically

$$\bar{M}_1 = \tfrac{1}{3}W + \tfrac{2}{3}(2W) = \tfrac{5}{3}W, \qquad (12)$$

where W is the needle width.

As a matter of fact the (110) dimensions are slightly smaller (305 Å for sample ii) than the apparent diameter measured by electron microscopy (330 Å). These discrepancies are still larger in the sedimented hematite. This question will be discussed later.

On the other hand, the mean (012)–(024), (104), and (116) sizes should be theoretically proportional to $t \sec\phi$, where t is the needle thickness. The thickness values calculated from this formula at 300°C show anyway that this dimension is smaller than the needle width, which confirms the microscopic observations. However, the wide range of these thickness values is not consistent with the above predictions. The same particles (ii) heated at 600°C show the best agreement with theory since the calculated thickness ranges from 100 Å (012)–(024) to 125 Å (104)–(116) so that the w/t ratio is between 1.5 and 2, as previously expected.

At 300°C, a Warren–Averbach diagram (Fig. 5a), where the $A(L)$ coefficients of the (012) and (024) reflections are plotted vs $1/d^2_{hkl}$ shows a negative slope from which a root-mean-squared strain has been estimated to be 5.5×10^{-3}. However, the true particle size coefficients obtained by extrapolating the function to $1/d^2_{(hkl)} = 0$ are close to the $A(M)$ coefficients of the (012) line so that the (012) mean size in Table II (110 Å) corresponds approximately to the "extrapolated" size whereas the (024)

TABLE II

MEAN PARTICLE SIZES $\bar{M}_1$ (Å) OBTAINED FROM X-RAY ANALYSIS

	Hematite sample					
				Acicular D		
Plane	Colloidal A	Colloidal B	Tabular C	300°C	600°C	600°C elutriated
(012)	—	—	—	110	190	—
(104)	250	120	50	85	160	255
(110)	270	190	150	280	305	370
(024)	265	135	60	105	185	240
(116)	270	140	75	190	170	310

mean particle size (105 Å) is a little more underestimated. Therefore although strains are present at 300°C, they do not affect consistently the peak broadening since the (012) and (024) dimensions are close together.

A similar Warren–Averbach plot for the samples heated at 600°C (Fig. 5b) shows that:

(i) The slope of $A(L)$ vs $1/d^2_{hkl}$ approaches close to zero. The strain broadening disappears at this temperature and the $A(L)$ coefficients can be considered as true particle or fault coefficients.

(ii) For each value of M, the extrapolated particle coefficients are greater at

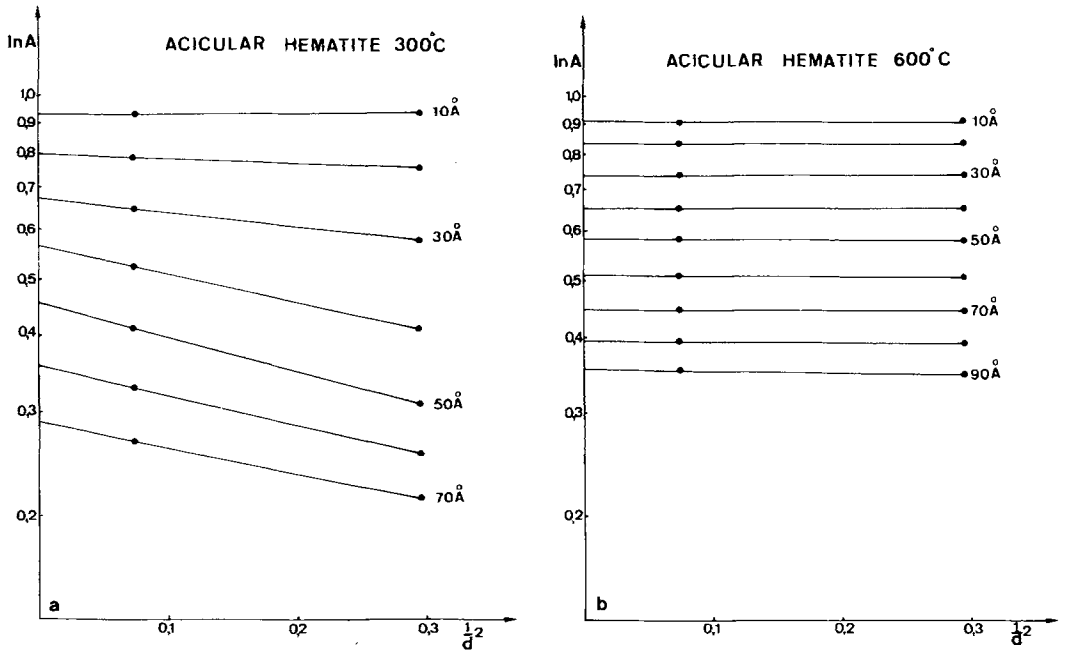

FIG. 5. Warren–Averbach plots of Fourier coefficients $A(L)$ of acicular hematite D as a function of $1/d^2$ for selected values of L. (a) After heating at 300°C. (b) After heating at 600°C.

600°C than at 300°C. Therefore, the decrease of the broadening of the (012) and (024) reflections in this temperature range is due to growth of the Bragg domains. The same conclusions are thought to be valid for the (104) reflection, which undergoes a broadening decrease between 300 and 600°C too large to be ascribed only to strain elimination.

Crystallite Size Distribution

Figure 6 enables us to compare the (110) particle size distributions $G(M)$ of samples at 300°C (i) and 600°C (ii) and of elutriated samples at 600°C (iii). At 300°C, the distribution which can be influenced by a weak strain broadening contribution is spread between a sharp peak at 40 Å and a well-separated peak at 500 Å. At 600°C, the only important modification involves the size fraction less than 200 Å of which the smallest sizes have grown to some extent. The removal of the smallest sizes by elutriation is shown very well in Fig. 6c which now includes two maxima. The first, at about 200 Å, has already appeared in Fig. 6b while the second, at 500 Å, is reinforced. As the size distribution is narrowed in the sedimented sample, it is believed that these two maxima correspond to the sizes expected in the (110) directions, i.e., the "width" size ($\frac{1}{3}$ of the planes) and the "double width size" ($\frac{2}{3}$ of the planes). In fact, the peak maxima are in a size ratio close to 2 : 1; moreover, the surface area of the second maximum reaches the same order of magnitude as the first; that is, closer to predictions assuming uniform-sized particles.

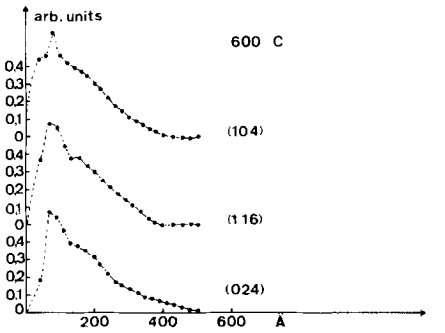

FIG. 7. Acicular hematite: Crystallite size distribution functions at 600°C.

Moreover, the second maximum at 500 Å is really specific of (110) directions since it does not appear in the same way along the "thickness" directions, i.e., the (024), (116), and (104) axes. The particle size distributions from these three reflections are shown at 600°C before and after elutriation in Figs. 7 and 8. In both figures, the peak shapes of the crystallite size distributions are similar: in nonsedimented hematite, a sharp peak is observed at about 75 Å in the three cases. A smooth maximum is then observed at ≃150 Å. In the sedi-

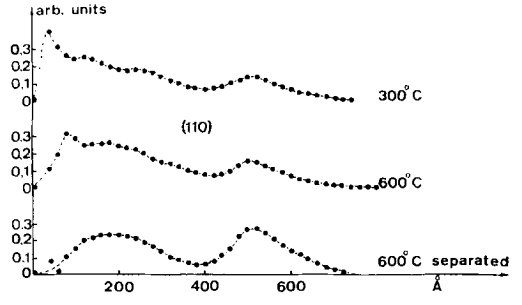

FIG. 6. Acicular hematite: (110) crystallite size distribution function G(L). (a) At 300°C. (b) At 600°C. (c) At 600°C after elutriation.

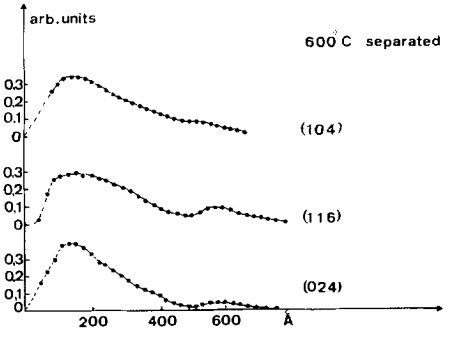

FIG. 8. Acicular hematite: crystallite size distribution functions at 600°C after elutriation.

mented hematite, the first peak has disappeared while the second remains at the same position. Thus the removal of the smallest particles by an elutriation process is correctly marked on the size distribution curves and therefore, the maxima observed are significant. Consequently, the nonuniform broadening still present at 600°C can be ascribed to the anisotropy of Bragg domains.

From the maxima in the distribution curves of sedimented hematite a width : thickness ratio can again be estimated. From the first maximum in the (110) distribution curve the average needle width should be 180 Å whereas the thickness calculated from the (104), (116), and (024) maxima corrected from angular functions ranges between 80 and 130 Å. A dimension ratio close to 2 : 1 is found again. It confirms the electron microscopy and the previous results of the mean sizes $\bar{M}_1$ as well.

Discussion

According to Lima de Faria (*4*) the powder pattern reflections with $h + k = 3n$ and $l = 3n$ remain sharp at low temperature whereas the others are diffuse. In fact, in *hcp* structures, stacking faults occur in the *c* direction so that line broadening arises from fault domains except for the planes obeying the above conditions, i.e., the $(11\bar{2}0)$, $(11\bar{2}3)$, $(11\bar{2}6)$, (300), etc., planes. Therefore, the nonuniform broadening observed at low temperature by this author was related to stacking faults in the packing of oxygen layers. On the other hand, the present size distribution curves at 300°C and at 600°C show that the broadening functions of (110) and (116) reflections which are supposed to be unaffected by faulting are quite different in hematite D. For example, in sedimented hematite, a more important fraction of smaller particles is observed in the (116) distribution. This can be ascribed to the finite ratio of particle width and thickness ($\simeq 2$) so that a part of the (116) planes, unlike the (110) planes, is cut by two perpendicular edges of the particles as shown in Fig. 9.

This example confirms that nonuniform broadening remains even at high temperature and can be explained by the anisotropy of particle shape rather than by faulting.

At low temperature, i.e., at $\simeq 300$°C, a weak contribution of strain broadening has been observed here for (012) and (024) reflections in hematite D.

On the other hand, it is likely that fault broadening can limit the crystallite sizes to some extent. Nevertheless, the good correlation between particle shape and nonuniform broadening in hematites A, B, C, and D suggests that, even at low temperature, the effect of particle shape anisotropy is predominant. The very weak broadening increment of the (104) and (024) reflections with respect to the (110) and (116) reflections observed in spherical-shaped particles of colloidal hematite A (Fig. 4a) probably gives an order of magnitude of faults present at low temperature.

The question whether the X-ray domain sizes correspond to the true particle dimensions is answered now. Although a good agreement is observed for "X-ray" and "microscopic" dimensions in colloidal hematite A, the former dimensions are generally less than the latter ones in acicular crystals, especially for the largest needles of elutriated hematite D.

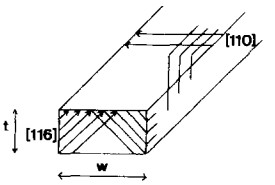

FIG. 9. Acicular hematite: two corresponding (110) and (116) directions are shown by arrows. The finite ratio of particle width and thickness (~2) shows that a fraction of (116) crystallite sizes are limited by the particle edges.

Lima de Faria (*4*) has pointed out that the main parameter change in goethite dehydration which is along of the goethite *c* axis (the $1\bar{1}0$ hematite axis) would be of the order of 3%.

As this author did not observe any significant contraction in this direction, he suggested that cracks would appear normal in this direction. Such facts are confirmed here since long-slit pores are observed normal to the needle width at 300°C. It is likely that these pores perturb the particle crystallinity and act as Bragg domain limits. At 600°C, these pores transform into closed spherical pores. An internal sintering occurs which brings about more crystal homogeneity so that a larger column fraction can reach the edges of the particles.

Irrespective to the "pore" effect limiting the domain sizes in the little acicular particles, it is thought that the large discrepancies between the "crystallite" and "microscopic" sizes after elutriation are related to needle clustering. Electron microdiffraction patterns of isolated large particles often show some sets of (*hkl*) spots close together on the same diffracted ring. Thus the large particles consist of several crystals which are slightly disoriented to each other. In this case the domain sizes could be limited either by the original goethite structure or by the dehydration process yielding a polycrystalline oxide as reported earlier by Goldsztaub (*1*).

Acknowledgments

The present research has been performed within a program supported by the belgian Fonds National de la Recherche Scientifique. The authors are also grateful to A. Le Bail and D. Louër for help and discussions. They thank Miss L. Van Helden and Mrs. C. Calvo-Roche for technical assistance.

References

1. M. S. Goldsztaub, *C.R. Acad. Sci.* **193,** 533 (1931).
2. H. P. Rooksby, *in* "X-ray Identification and Crystal Structures of Clay Minerals" (G. W. Brindley, Ed.), Chap. 10 (1951).
3. M. H. Francombe and H. P. Rooksby, *Clay Miner. Bull.* **4,** 1–14 (1959).
4. J. Lima de Faria, *Z. Kristallogr. Kristallgeometrie* **119,** 176 (1973).
5. G. W. Brindley, *in* "Progress in Ceramic Science" (J. E. Burke, Ed.), Vol. 3 Chap. 1 (1963).
6. J. D. Bernal, D. R. Dasgupta, and A. L. Mackay, *Clay Miner. Bull.* **4,** 15–30 (1959).
7. B. E. Warren, and B. L. Averbach, *J. Appl. Phys.* **23,** 497, (1952).
8. E. F. Bertaut, *Acta Crystallogr.* **3,** 14 (1950).
9. B. E. Warren, and B. L. Averbach, *J. Appl. Phys.* **21,** 595 (1950).
10. B. E. Warren, *Progr. Metal Phys.* **8,** 147 (1959).
11. P. Scherrer, *Nachr. Ges. Wiss. Göttingen,* 98–100 (1918).
12. A. R. Stokes, *Proc. Phys. Soc. (London) B* **61,** 382 (1948).
13. R. A. Young, R. J. Gerdes, and A. C. J. Wilson, *Acta Crystallogr.* **22,** 155 (1967).
14. A. Bienenstock, *J. Appl. Phys.* **34,** 1391 (1963).
15. F. Hossfeld, and H. J. Oel, *Z. Angew. Phys.* **20, 6,** 493–498, (1966).
16. F. de Bergevin, and P. Germi, *J. Appl. Crystallogr.* **5,** 416–420 (1972).
17. B. Moraweck, P. de Montgolfier, and A. J. Renouprez, *J. Appl. Crystallogr.* **10,** 191–196 (1977).
18. G. Tomandl, *Sci. Ceram.* **8,** 145–158 (1976).
19. A. Le Bail, and D. Louër, *J. Appl. Crystallogr.*, **11,** 50–55 (1978).
20. R. J. De Angelis, *in* "Local Atomic Arrangements Studied by X-Ray Diffraction," Vol. 36, p. 271, Metallurgical Society Conferences, Chicago (1965).
21. A. Guinier, "Théorie et technique de la radiocristallographie," Dunod, Paris (1964).
22. R. Derie, P. H. Duvigneaud, and L. Van Helden, "4ème Colloque Int. sur les méthodes analytiques par rayonnement X, Strasbourg, 9–13 mai 1977."